Magnetic microscopy of skyrmions in magnetic thin films with chiral overlayers

Buddhika Hondamuni,[1,2,*] Théo Balland,[1] Fabian Kammerbauer,[1] Ashish Moharana,[1] Bindu,[3] Amandeep Singh,[3] Meital Ozeri,[3] Shira Yochelis,[3] Yossi Paltiel,[3] Omkar Dhungel,[1,2] Zeeshawn Kazi,[4] Kai-Mei C. Fu,[5,6] Hideyuki Watanabe,[7] Mathias Kläui,[1] Arne Wickenbrock,[1,2,8] Nir Bar-Gill,[3,9] Angela Wittmann,[1] and Dmitry Budker[1,2,8,10,†]

[1]*Institute of Physics, Johannes Gutenberg-Universität Mainz, 55099 Mainz, Germany*
[2]*Helmholtz Institute Mainz, Staudingerweg 18, 55128 Mainz, Germany*
[3]*Institute of Applied Physics, The Hebrew University of Jerusalem, Jerusalem 9190401, Israel*
[4]*Princeton University, Department of Electrical and Computer Engineering, Princeton, New Jersey 08544, USA*
[5]*Department of Physics, University of Washington, Seattle, WA 98195-1560, USA*
[6]*Electrical and Computer Engineering Department, University of Washington, Seattle, Washington 98105, USA*
[7]*National Institute of Advanced Industrial Science and Technology (AIST), Tsukuba Central 2, 1-1-1, Umezono, Tsukuba, Ibaraki 305-8568, Japan*
[8]*GSI Helmholtzzentrum für Schwerionenforschung GmbH, 64291 Darmstadt, Germany*
[9]*Racah Institute of Physics, The Hebrew University of Jerusalem, Jerusalem 9190401, Israel*
[10]*Department of Physics, University of California, Berkeley, California 94720, USA*

(Received 23 April 2026; revised 10 August 2026; accepted 22 September 2026; published 26 October 2026)

Topologically nontrivial magnetic textures such as skyrmions offer promising opportunities for spintronic applications. In recent years, it has been shown that the magnetic properties of layered materials can be affected by depositing chiral molecules on the surface, while the influence of chiral overlayers on skyrmion properties such as their stability and interactions remains largely unexplored. To address this challenge, we employ wide-field nitrogen-vacancy (N-V) magnetometry to directly image skyrmions in chiral-molecule-functionalized magnetic thin films, enabling quantitative mapping of magnetic stray fields over extended areas under ambient conditions. Using pixel-resolved optically detected magnetic resonance (ODMR) combined with controlled magnetic fields, we reproducibly nucleate and probe skyrmion states in CoFeB ferromagnetic samples, enabling quantitative investigation of their properties. We observe indications of enantioselective and magnetic-field-polarity-dependent modifications of skyrmion properties suggesting possible chirality-dependent modifications of topological spin textures and motivating future theoretical investigations of the underlying coupling mechanisms.

DOI: 10.1103/thmz-53f2

I. INTRODUCTION

Magnetic skyrmions are nanoscale topological spin textures [1] that have attracted considerable interest for next-generation spintronic technologies due to their stability [2], small size [3], and efficient manipulation by external stimuli such as magnetic fields and electric currents [4–6]. In parallel, recent advances have demonstrated the existence of new classes of topological magnetic textures beyond conventional skyrmions, including electrically generated magnetic heliknotons and other higher-order topological states [7], further enriching the landscape of topological magnetism. Understanding how to control these topologically nontrivial spin configurations is therefore of both fundamental and technological importance.

Thin film magnetic systems support nanoscale domain structures and skyrmions that are particularly relevant for high-density magnetic storage applications [8–10]. Their magnetic properties can be engineered through interface design, multilayer stacking [11], and strain [12], enabling control over domain formation, stability, and dynamics [13]. Consequently, magnetic thin films provide a versatile platform for investigating controllable topological spin textures.

An emerging direction for controlling magnetic textures involves the interaction between magnetic materials and

*Contact author: hondamub@uni-mainz.de
†Contact author: budker@uni-mainz.de

Published by the American Physical Society under the terms of the Creative Commons Attribution 4.0 International license. Further distribution of this work must maintain attribution to the author(s) and the published article's title, journal citation, and DOI.

chiral molecules. The chirality-induced spin selectivity (CISS) effect demonstrates that electron spin polarization can depend on molecular handedness [14]. Chiral molecules have been shown to influence magnetic behavior [15], chemical reactivity, and spin-dependent electron transport. In particular, enantioselective adsorption of chiral molecules on ferromagnetic surfaces has been shown to depend on the substrate magnetization direction, indicating a coupling between molecular chirality and magnetic order [16]. Such interactions suggest that molecular chirality may modify magnetic domain configurations and stabilize specific spin textures, offering a route toward functional hybrid molecular-magnetic systems [17].

Recent experiments using magneto-optical Kerr effect (MOKE) microscopy have explored this interaction in magnetic multilayer functionalized with chiral polypeptides. These studies demonstrate that adsorption of chiral molecules can modify magnetic properties, such as coercivity, domain pinning, and magnetic anisotropy, and can influence the formation and stability of magnetic domains [17,18]. However, MOKE imaging primarily probes magnetization contrast and does not provide direct, quantitative information about the stray magnetic fields generated by the underlying spin textures, limiting access to the local magnetic energy landscape.

Understanding how chiral molecules influence skyrmion properties therefore requires experimental techniques capable of quantitatively mapping stray magnetic fields associated with magnetic textures over extended areas. Scanning single N-V magnetometry offers nanoscale spatial resolution and high magnetic sensitivity, but the sequential scanning approach typically restricts the field of view (FOV) to a few micrometers and leads to long acquisition times when imaging extended magnetic textures.

Wide-field N-V magnetometry provides a complementary approach by enabling parallel optical detection of optically detected magnetic resonance (ODMR) from ensembles of near-surface N-V^- centers in diamond. This technique allows quantitative imaging of static stray magnetic fields with sub-micrometer spatial resolution over FOVs spanning tens of micrometers under ambient conditions [19,20]. Previous studies combining wide-field N-V sensing with magneto-optical measurements have visualized stripe domains in multilayer ferromagnet [21], while complementary experiments using N-V magnetometry and related nanoscale probes have revealed detailed properties of skyrmions and domain structures in ultrathin magnetic films and multilayers [22–26]. More broadly, N-V magnetometry has been applied to visualize stray magnetic fields in ferromagnetic films, magnetic nanoparticles, biological systems, and superconducting vortices, as well as to reconstruct current densities in electronic and mesoscopic devices [27–34].

In this work, we use wide-field continuous-wave (cw) N-V^- center magnetometry to quantitatively image the stray magnetic fields of skyrmions in multilayer ferromagnet functionalized with chiral α-helix poly-alanine molecules under ambient conditions. By directly comparing molecule-functionalized and nonfunctionalized regions of the same sample, we access spatial variations in skyrmion properties through their stray-field signatures, enabling a quantitative investigation of possible chirality-dependent modifications of the local magnetic energy landscape. This approach provides information that is not accessible with conventional MOKE imaging and complements scanning probe techniques by combining quantitative field reconstruction with a large FOV. In the present implementation, the magnetic image is acquired in approximately 10 min. While the acquisition time could be reduced by decreasing the number of sampled frequency points, we intentionally employ dense spectral sampling with averaging to enhance the signal-to-noise ratio and enable robust pixel-wise ODMR fitting, thereby improving the reliability and quality of the reconstructed magnetic field maps.

II. TOPOLOGICAL DEFECTS IN ORDERED MAGNETS

Magnetic materials undergo a transition from a paramagnetic state with randomly oriented spins to an ordered phase with finite magnetization below a critical temperature. This spontaneous symmetry breaking establishes long-range magnetic order and enables the formation of spatially structured spin textures, including topological defects [35]. Owing to their nontrivial topology and nanoscale size, skyrmions are of particular interest for both fundamental studies and spintronic applications. A skyrmion is characterized by a continuous rotation of the magnetization that wraps the unit sphere, leading to a quantized topological charge (winding number) [6,13,36]. Their stability results from the competition among exchange interaction, magnetic anisotropy, Zeeman energy, and the Dzyaloshinskii-Moriya interaction (DMI), which favors chiral spin textures. Depending on whether the DMI is interfacial or bulk in origin, Néel-type or Bloch-type skyrmions can form. These configurations may appear either as metastable states or as global energy minima, depending on material parameters, applied field, and geometry [3,37–42].

III. MAGNETO-CHIRAL EFFECT

Control of skyrmions through external magnetic fields, currents, and interfacial engineering is well established [6]. An emerging approach exploits molecular chirality, which represents *true* chirality in the symmetry sense and introduces structural handedness. In contrast, magnetization corresponds to a form of *false* chirality, and their

coexistence enables hybrid magneto-chiral systems [17,43]. Chiral molecules, which are not super-imposable on their mirror images, can influence spin-dependent processes through the CISS effect, where electron transmission becomes spin selective [44–46]. While CISS is commonly studied in transport geometries, chiral molecular overlayers on magnetic thin films can induce enantiomer-dependent modifications of magnetic properties [47]. Within a symmetry-based framework, the broken spatial inversion symmetry introduced by molecular chirality can modify effective magnetic coupling to the magnetic layer and thus affect the spin textures. Consistent with this picture, enantioselective adsorption of chiral molecules has been shown to modify magnetic properties at the surfaces of ferromagnetic materials, including coercivity, magnetic anisotropy, and domain behavior [18]. Here, we interpret the handedness- and polarity-dependent changes in skyrmion properties as being consistent with chirality-dependent modifications of the interfacial magnetic energy landscape. Several possible microscopic mechanisms may contribute to such behavior. First, adsorption of chiral molecules may induce a finite interfacial spin density through the CISS effect, leading to weak exchange coupling with the magnetic layer. Second, chiral molecules may facilitate anharmonic lattice excitations or chiral phonon modes that mediate coupling across the molecular overlayer and magnetic film. Third, the molecular adsorption breaks structural inversion symmetry and may modify interfacial Rashba spin-orbit coupling and associated magnetic interactions. At present, however, it is not possible to determine which of these mechanisms dominates in our system under study.

IV. MAGNETIC SAMPLES AND CHIRAL MOLECULES

The materials studied here are thin films with perpendicular magnetic anisotropy (PMA), in which the magnetization preferentially aligns normal to the film plane. They form complex domain patterns under applied bias fields. The multilayer films were deposited by dc magnetron sputtering using a Singulus Rotaris deposition tool with the structure $Si/Si(100)/Ta(4)/[Co_{20}Fe_{60}B_{20}(0.9)/Ta(0.08)/MgO(2)/Ta(2)]_2/Ta(2)$, where numbers in parentheses denote the layer thickness in nanometers [Fig. 1(a)]. This stack supports PMA and stabilizes magnetic domains suitable for skyrmion formation. As the chiral overlayer, we employ α-helix poly-alanine (AHPA) polypeptide, which is known to induce strong domain pinning and a localized increase in coercive field [17]. The molecules have a purity of approximately 95%, terminate in a surface $-$OH group and possess a calculated molecular mass of 3008.6 g/mol. The molecular solution was prepared at a concentration of 1 mM in ethanol.

V. EXPERIMENTAL METHODS

To minimize sample-to-sample variations, selectively functionalized samples containing adjacent molecule-functionalized and nonfunctionalized regions were employed. The samples were prepared using a poly-methyl methacrylate (PMMA)-assisted masking procedure, whereby one half of the Au-capped magnetic multilayer was exposed to overnight adsorption of D- or L-AHPA molecules, while the remaining half served as a reference region. Molecular adsorption and handedness were verified by circular dichroism spectroscopy and contact-angle measurements [Figs. 1(b) and 1(c)].

Magnetic skyrmions were nucleated by applying a transient in-plane (IP) magnetic field pulse in the presence of an OOP bias field, resulting in isolated skyrmions stabilized within the PMA multilayer. The resulting magnetic textures were imaged using wide-field N-V magnetometry. Spatially resolved ODMR measurements were performed by sweeping the MW frequency around the N-V zero-field splitting and recording fluorescence images at each frequency point [Fig. 1(d)]. Pixel-wise fitting of the ODMR spectra enabled reconstruction of two-dimensional maps of the N-V-projected stray magnetic field, $B_{\text{N-}V}$, over the FOV.

VI. RESULTS AND DISCUSSION

Figure 2 presents N-V stray-magnetic field maps of magnetic domain configurations, illustrating the evolution from stripe domains to isolated skyrmions under an applied OOP magnetic field. The measured signal corresponds to the projection of the magnetic field along the N-V axis, so that the reconstructed maps represent a weighted combination of IP and OOP stray-field components. For thin films with PMA, the stray field above the sample is dominated by the OOP component, such that $B_{\text{N-}V}$ provides a reliable proxy for B_z up to a geometric scaling factor. We note that no full vector-field or magnetization reconstruction is performed in this work. Such reconstruction would require measurements along multiple N-V orientations or inverse modeling, which is beyond the scope of the present study.

Magnetic stripes are nucleated by applying a brief (approximately 1 s) IP magnetic field pulse of approximately 30 mT using a laterally movable permanent magnet while maintaining a constant OOP bias field. This pulse destabilizes the stripe domain walls (DWs), enabling the formation of skyrmions. After removal of the IP field, the resulting magnetic configuration depends on the OOP field, intrinsic sample parameters, and temperature. The combined use of controlled OOP bias and transient IP excitation provides a reliable method for generating the skyrmion phase.

Following this preparation, the domain morphology undergoes a systematic evolution as the OOP field

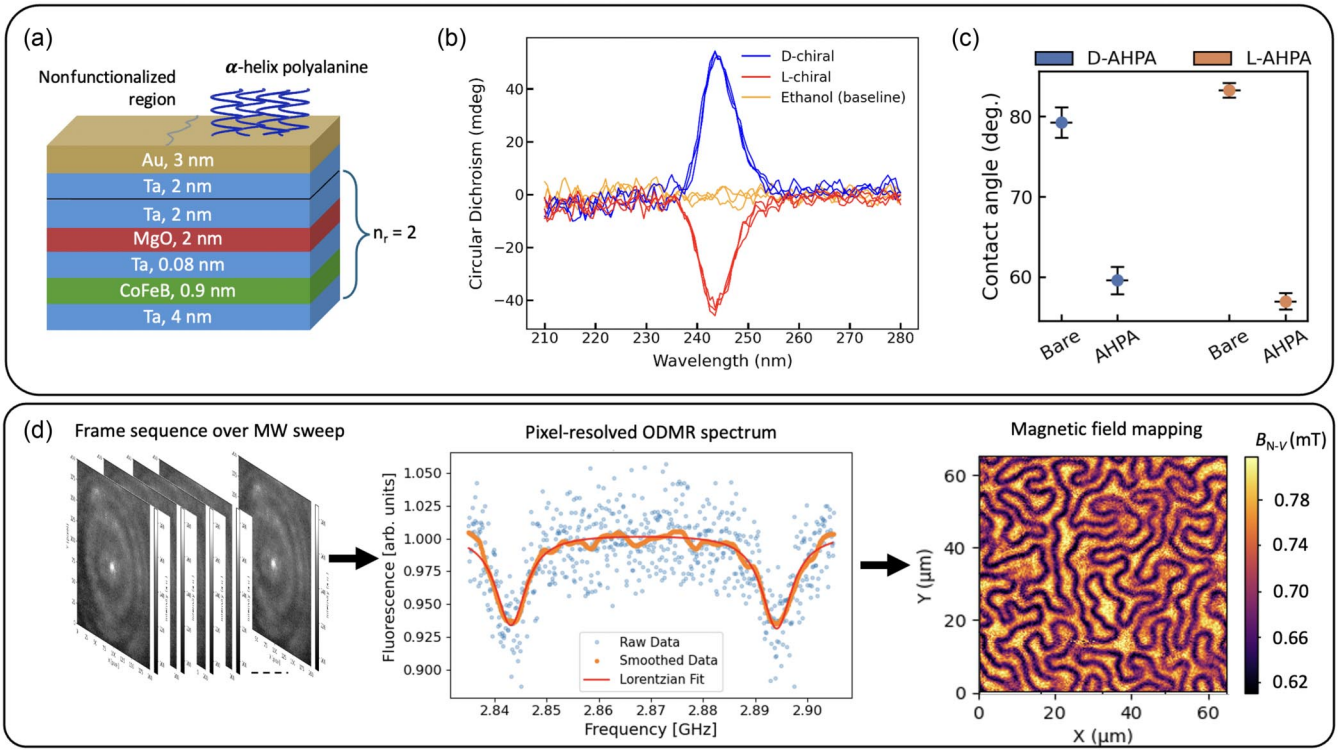


FIG. 1. (a) Sample design: Schematic of the multilayer magnetic stack with a approximately 3 nm Au capping layer, where chiral molecules are deposited on only half of the surface, leaving an adjacent nonfunctionalized region for direct comparison. Molecular characterization: (b) Circular dichroism (CD) spectra of D- and L-AHPA solutions measured in the UV range (210–280 nm), showing mirror-symmetric extrema near approximately 240–245 nm that confirm opposite molecular handedness; the ethanol reference remains close to zero. (c) Contact angle measurements for bare and molecule-functionalized regions, demonstrating the change in surface wettability after adsorption of D-AHPA and L-AHPA molecules. (d) N-V magnetometry workflow: A sequence of photoluminescence frames acquired during a microwave (MW) frequency sweep yields pixel-resolved ODMR spectra for the FOV, and each spectrum is fitted with a Lorentzian function to determine the resonance positions and splitting, enabling quantitative reconstruction of the stray magnetic field map.

increases. At low fields ($B_z \approx 1.40$–1.50 mT), the film exhibits a dense labyrinthine stripe-domain phase. At $B_z \approx 1.55$ mT, the stripes are narrow and fragment, producing a mixed state of broken stripes and emerging circular textures that signal the onset of skyrmion nucleation. At higher fields ($B_z \approx 1.57$–1.59 mT), isolated skyrmions dominate the magnetic contrast, appearing as individual circular textures embedded in a nearly uniform background and stabilized at defect-induced pinning sites commonly present in thin magnetic films [10]. When the field reaches $B_z \approx 1.61$ mT, most stripe domains vanish and only isolated skyrmions remain, indicating a skyrmion-dominated phase close to magnetic saturation. At $B_z \approx 1.68$ mT, the magnetic contrast diminishes as the film approaches magnetic saturation, and the fluorescence signal becomes nearly uniform. Such field-driven transitions from stripe domains to isolated skyrmions and ultimately to the saturated state are expected in PMA thin films and arise from the competition between exchange, magnetic anisotropy, dipolar interactions, and Zeeman energy [1,8].

To characterize the spatial extent of the observed magnetic textures, we extract multiple line profiles of the projected stray magnetic field $B_{\text{N-}V}$ across representative features [Fig. 3]. The extracted full width at half maximum (FWHM) serves as an effective measure of the apparent texture size. Since the measured signal represents a convolution of the underlying magnetization with the dipolar stray-field response and is further broadened by the finite N-V-sample stand-off distance and sensing-layer thickness [48], the FWHM should not be regarded as the intrinsic skyrmion diameter. Instead, it is employed here only as an effective quantity for relative comparisons of magnetic texture sizes under identical experimental conditions. Figure 3 summarizes the distributions of the extracted FWHM values for the two representative magnetic-field conditions.

To evaluate the influence of molecular chirality on skyrmion properties, we performed a statistical analysis of the skyrmion density [Fig. 4], effective skyrmion diameter, nearest-neighbor skyrmion-skyrmion (Sk-Sk) distance, and shape factor for molecule-functionalized and

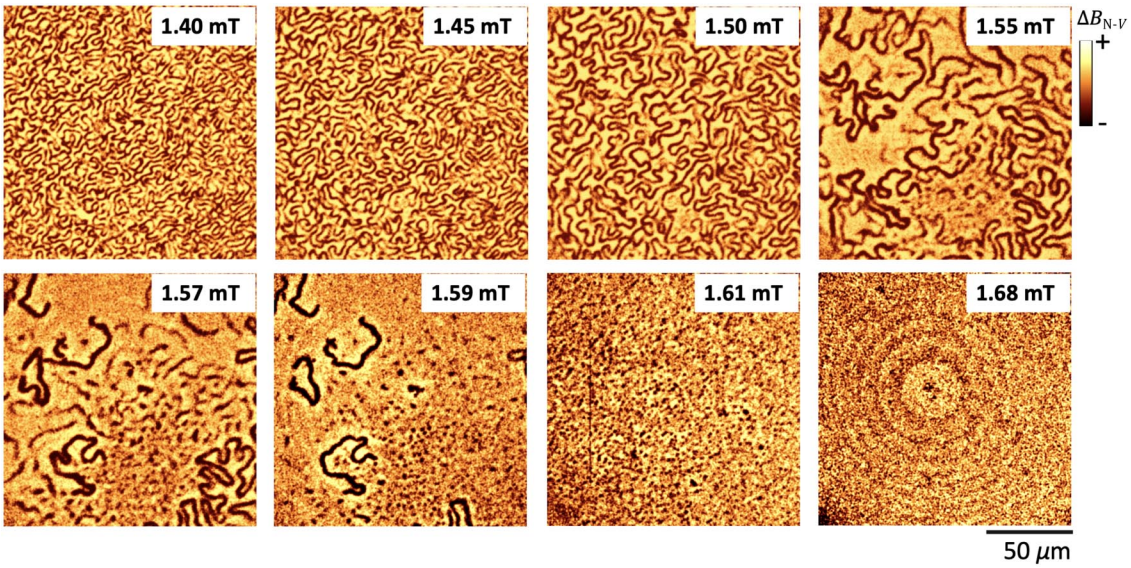


FIG. 2. Evolution of magnetic domains to skyrmion phase in CoFeB thin film under increasing B_z field. Background-subtracted N-V magnetic field maps ($\Delta B_{N\text{-}V}$) reveal the progressive deformation and coalescence of skyrmions together with stripe domains with increasing out-of-plane (OOP) field. The magnetic contrast is normalized by the standard deviation σ (approximately 1.15 μT) of the field distribution, so that the color scale reflects statistically significant deviations from the background. The faint concentric ring pattern originates from optical interference caused by reflections within the diamond.

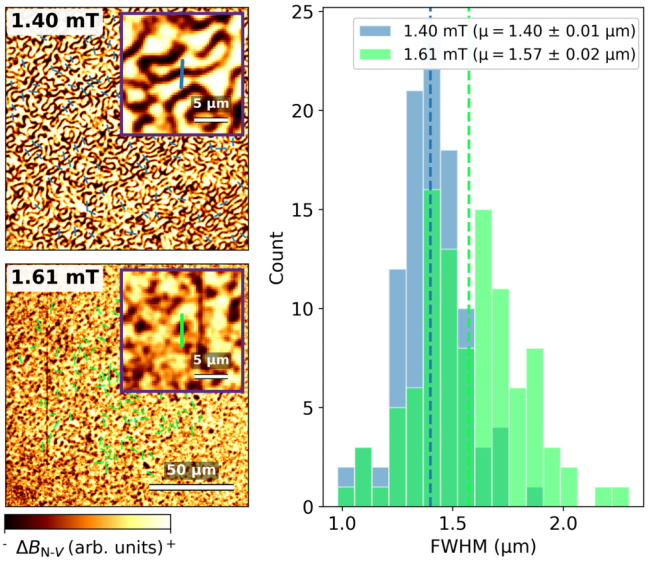


FIG. 3. Statistical distribution of effective magnetic texture sizes. Representative $B_{N\text{-}V}$ maps acquired at OOP magnetic fields of 1.40 and 1.61 mT, with inset panels showing magnified views of representative magnetic textures. Multiple lateral line profiles were extracted across these textures, and their FWHM was used as an effective measure of the apparent texture size. Histograms summarize the extracted FWHM values for both magnetic fields, with dashed lines indicating the corresponding mean values.

nonfunctionalized regions under opposite magnetic field polarities ($B_z = \pm 1.6$ mT). Because the field is obtained from the resonance splitting, the absolute sign of the N-V-projected field is not resolved. The positive and negative values shown in $\Delta B_{N\text{-}V}$ therefore represent deviations from the background/reference field rather than the absolute field direction.

The study was performed using two independently prepared selectively functionalized samples, one functionalized with D-AHPA and the other with L-AHPA molecules. For each sample, three independent FOVs were analyzed over two repeated skyrmion nucleation cycles, yielding six FOV-by-cycle observations for each experimental condition and magnetic-field polarity. Statistical comparisons were performed at the FOV-by-cycle level [Table I], with one value per FOV per nucleation cycle. Individual skyrmions were used only to calculate the corresponding FOV-level metrics, including skyrmion density, mean diameter, mean shape factor, and mean nearest-neighbor spacing. For each condition, the total number of analyzed skyrmions is reported together with the mean and its 95% confidence interval (CI), which quantify the average value and the uncertainty of the estimated population mean. Within- and between-cycle variances are reported to distinguish the intrinsic spatial variability within a nucleation cycle from the reproducibility of the measurements between independent nucleation events, thereby assessing experimental stability. Differences between functionalized and nonfunctionalized regions were evaluated using the Mann-Whitney U test, a nonparametric statistical test that determines whether the two groups originate from the same underlying distribution without assuming normality. Cohen's d effect size was additionally calculated to quantify the magnitude of the observed differences independently of sample size,

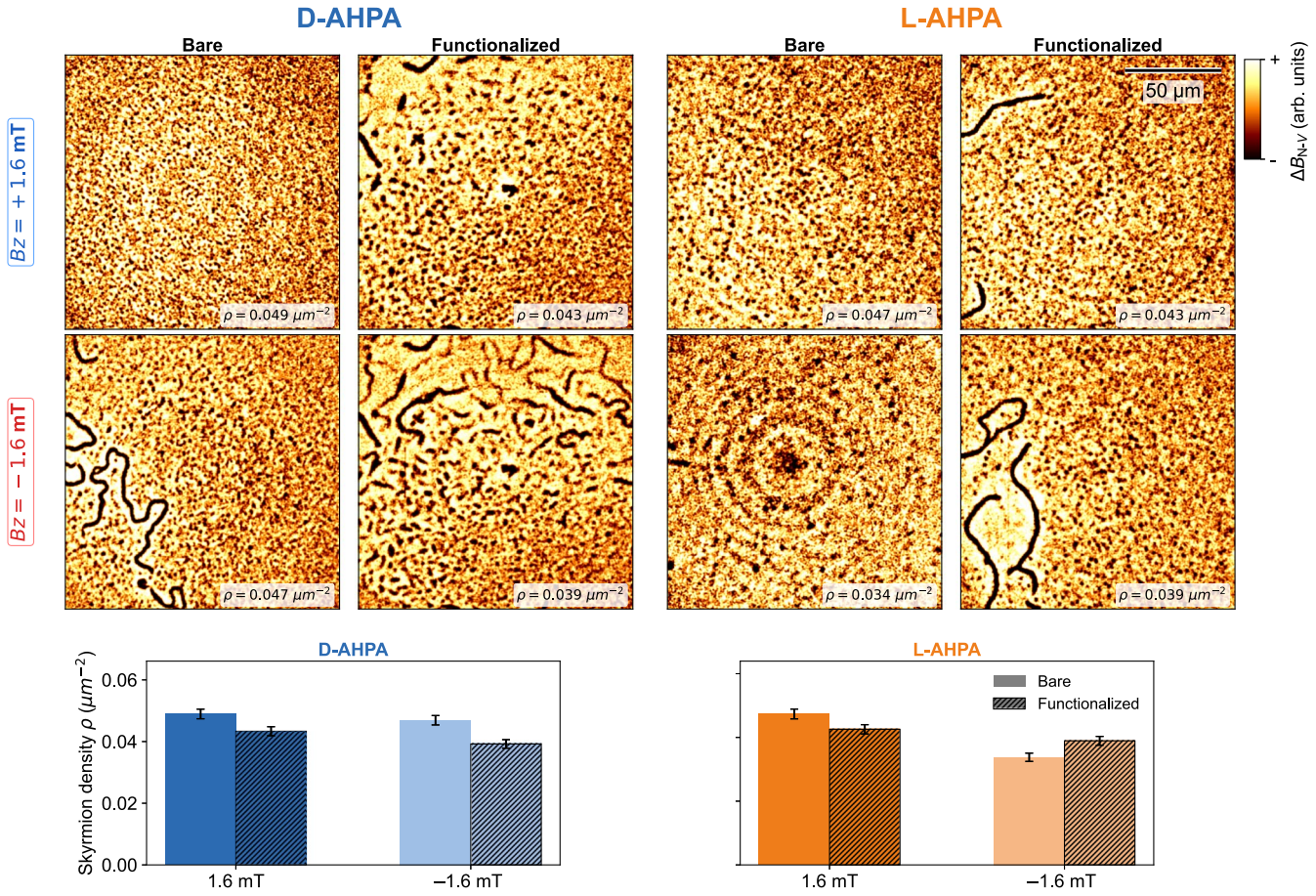


FIG. 4. Representative N-V magnetic images and statistical comparison of skyrmion densities in chiral-molecule-functionalized regions. Stray magnetic field maps ($\Delta B_{\text{N-}V}$) acquired under $B_z = \pm 1.6$ mT after application of a approximately 30 mT IP magnetic pulse are shown for bare and selectively functionalized regions of D-AHPA and L-AHPA samples. The extracted skyrmion density ρ is indicated in each panel. The lower plots summarize the average skyrmion densities within the corresponding FOVs.

thereby distinguishing statistically meaningful changes from negligible ones. Because the molecule-functionalized and reference regions coexist on the same substrate, all comparisons were performed under identical growth, magnetic-history, and measurement conditions, thereby minimizing systematic sample-to-sample variations.

Skyrmions were identified from the reconstructed stray-field images using a previously validated U-Net-based segmentation framework for magnetic texture analysis [49]. The complete training datasets and pretrained models are publicly available in the repository of Winkler *et al.* [50]. The resulting segmentation masks were used to determine skyrmion positions and geometrical properties for subsequent statistical analysis.

Detailed statistical results supporting the quantitative analysis are provided in Appendix D. Across the investigated observables, the molecule-functionalized regions exhibit trends that depend on both molecular handedness and magnetic-field polarity. However, the magnitude of these differences is generally comparable to the variability introduced by stochastic skyrmion nucleation and local pinning. Consistent with this observation, most 95% CIs for the mean differences overlap zero, the Mann-Whitney U tests do not generally satisfy the conventional significance criterion ($p < 0.05$), and the corresponding effect sizes remain small to moderate. These results indicate that, within the present dataset, the observed variations should be interpreted as suggestive trends rather than statistically conclusive evidence of chirality-induced modifications.

The analysis further demonstrates that repeated nucleation cycles introduce measurable variations in skyrmion density and morphology, highlighting the influence of stochastic nucleation and local pinning. Incorporating repeated nucleation cycles and independent FOVs therefore enables a more reliable evaluation of the observed chirality- and polarity-dependent trends. In thin films, skyrmion size, spacing, and morphology are governed by the interplay between interfacial DMI, PMA, dipolar interactions, and defect-induced pinning [2,3,51]. The experimentally observed trends are therefore consistent with possible chirality-dependent perturbations of the

interfacial magnetic energy landscape. However, the present measurements do not permit identification of a unique microscopic mechanism, and distinguishing the individual contributions from DMI, anisotropy, dipolar interactions, and pinning will require complementary experiments, theoretical modeling, and micromagnetic simulations, which are beyond the scope of the present work.

VII. CONCLUSIONS

We demonstrate wide-field N-V magnetometry of chiral-molecule-functionalized magnetic thin films with perpendicular magnetic anisotropy, enabling direct microscale imaging and quantitative analysis of skyrmion configurations under identical experimental conditions. Our statistical analysis reveals indications of enantioselective and magnetic-field-polarity-dependent modifications of skyrmion properties, while also demonstrating that a significant fraction of the observed variability originates from stochastic skyrmion nucleation and local pinning. The observed asymmetry under magnetic-field reversal suggests that molecular adsorption affects one or more interfacial magnetic parameters governing skyrmion formation.

The present results should be regarded as experimentally motivated indications rather than definitive evidence of a specific magneto-chiral coupling mechanism. Complementary magneto-optical measurements performed on the same selectively functionalized samples provide further evidence for chirality-dependent perturbations of the magnetic energy landscape and are currently being prepared for publication elsewhere. Identifying the individual contributions from Dzyaloshinskii-Moriya interaction, magnetic anisotropy, and pinning remains beyond the scope of the present work. Overall, the present study establishes wide-field N-V magnetometry as a versatile platform for probing possible chirality-dependent modifications of topological spin textures and provides motivation for future theoretical and experimental investigations.

ACKNOWLEDGMENTS

This work was supported by the Carl Zeiss Stiftung (HYMMS Project No. P2022-03-044), the EU project HEU-RIA-MUQUABIS (Grant Agreement No. 101070546), the MPGC with JGU, the Deutsche Forschungsgemeinschaft (DFG, German Research Foundation) through FKZ: SFB 1552/1 (Project No. 465145163) and ASPIRE Joint Japan-Germany Quantum Technologies program. K.C.F. acknowledges support from the University of Washington Molecular Engineering and Materials Center, funded by the National Science Foundation (NSF) Materials Research Science and Engineering Centers (MRSEC) program (Grant No. DMR-2308979). T.B., F.K., and M.K. acknowledge support from the DFG through SPP 2137 (Project No. 403502522) and TRR 173 Spin+X (Projects A01, A12, and B02). The authors also acknowledge funding from TopDyn.

This project received funding from the European Research Council (ERC) under the European Union's Horizon 2020 research and innovation program (Grant No. 856538, project "3D MAGiC", and Grant No. 101070290, project "NIMFEIA"), as well as from the Marie Sklodowska-Curie grant agreement No. 101119608 ("TOPOCOM"). Ar.W. acknowledges support from the German Federal Ministry of Research, Technology and Space (BMFTR) within the Quantum Technologies program via the DIAQNOS puoject (Project No. 13N16455). In addition, this work was supported by the Ministerium für Wirtschaft, Arbeit und Tourismus (InvestBW), project VitalQ (BW811662170), and by the Helmholtz Association through the projects Quantum Sensing for Fundamental Physics (QS4Physics) from the Innovation Pool of the research field Helmholtz Matter, QuBattery, and QuBiopsy. A.M. and An.W. acknowledge support from the DFG through TRR 173 Spin+X (Projects A09 and B14). Finally, the authors thank Muhib Omar and Jonas Raabe for their valuable technical support and assistance with programming throughout this work.

DATA AVAILABILITY

The data and codes supporting the findings of this article are openly available on Zenodo [52].

APPENDIX A: N-V WIDE-FIELD MAGNETIC IMAGING

N-V^- centers in diamond possess optically addressable electron spin states that can be initialized, coherently manipulated, and read out at room temperature [54,55]. Ensembles of near-surface N-V^- centers enable minimally invasive, real-space magnetic imaging over tens to hundreds of micrometers with sub-micrometer spatial resolution [19,20], providing access to complex magnetic textures such as skyrmions that are difficult to investigate using bulk techniques including SQUID, vibrating sample magnetometry, and x-ray scattering [32,56,57].

Figure 5(a) shows the energy-level structure of the N-V^- center. The electronic ground state is a spin-triplet $(S=1)^3A_2$ state with sublevels $m_s = 0, \pm 1$, separated by a zero-field splitting of $D \approx 2.87$ GHz [55]. Optical excitation at $\lambda = 532$ nm polarizes the spin into the $m_s = 0$ state, while spin-dependent photoluminescence

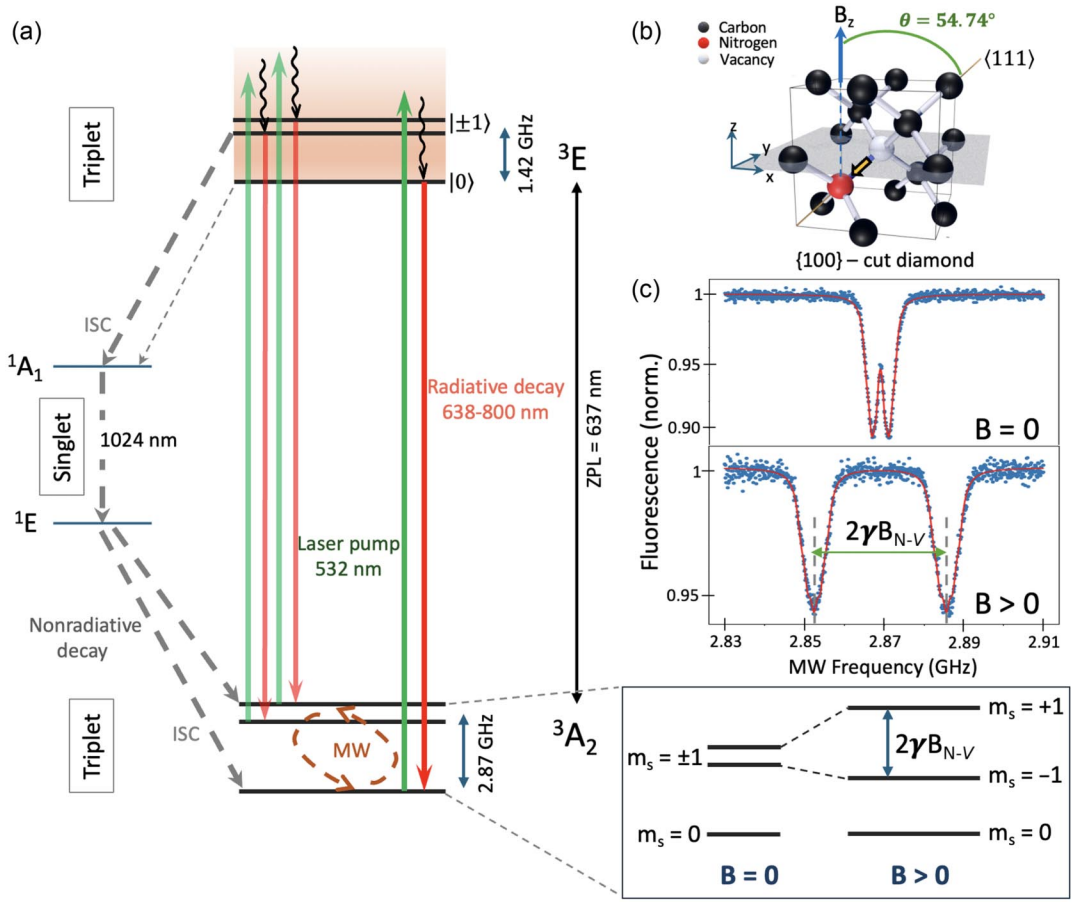


FIG. 5. (a) Energy-level diagram of the N-V^- center. The N-V^- center has a spin-1 ground-state triplet, $^3A_2$; within this manifold, the $m_s = 0$ and $m_s = \pm 1$ sublevels are split by the zero-field splitting $D \approx 2.87$ GHz at room temperature (this splitting is internal to the ground triplet). The center also has an excited triplet state, ^{3}E; optical transitions between $^3A_2$ and ^{3}E (zero-phonon line at approximately 637 nm) are used for optical excitation and readout. Continuous-wave 532 nm green laser excitation pumps population from $^3A_2$ to ^{3}E. Relaxation back to the ground state occurs either via radiative (optically allowed) decay or via spin-selective nonradiative decay through intermediate singlet states, which gives rise to spin-dependent fluorescence contrast. Dashed arrows indicate nonradiative or spin-nonconserving pathways. Spin sublevels are labeled by their magnetic quantum numbers ($m_s = 0, \pm 1$). MW control enables coherent spin manipulation between these sublevels, and an external magnetic field causes Zeeman splitting of the $m_s = \pm 1$ sublevels. (b) $\{100\}$-cut diamond lattice. The N-V center direction (orange arrow) along $\langle 111 \rangle$ and the applied magnetic field B_z (surface normal) [53]. (c) ODMR spectra of the N-V center; the upper plot shows the resonance at zero magnetic field ($B = 0$). The lower plot shows the Zeeman splitting under a finite magnetic field ($B > 0$), where the resonance splits into two peaks separated by $2\gamma B_{\text{N-}V}$, where γ is the gyromagnetic ratio (28.024 GHz/T).

(PL) enables optical readout since the $m_s = 0$ state exhibits higher PL intensity than the $m_s = \pm 1$ states [55].

Applying a magnetic field along the N-V axis [Fig. 5(b)] lifts the degeneracy of the $m_s = \pm 1$ states through the Zeeman effect. ODMR is observed by sweeping a MW field across the spin resonances while monitoring the PL signal [19]. At zero magnetic field, a small residual splitting [Fig. 5(c)] may arise from crystal strain or local electric fields [55,58]. In high-quality diamond samples, the hyperfine interaction with the ^{14}N nuclear spin ($I = 1$) can further produce a characteristic triplet splitting of approximately 2.16 MHz [55]. In the present measurements, however, this hyperfine structure is not resolved.

Wide-field magnetic imaging is performed by recording spatially resolved ODMR spectra from an ensemble of near-surface N-V^- centers. Continuous-wave 532 nm laser excitation (approximately 70 mW) polarizes the spins, while the MW frequency is swept around 2.87 GHz. At each frequency point, a fluorescence image is recorded using an sCMOS camera, yielding an ODMR image stack.

To suppress common-mode fluctuations arising from laser-power variations and camera drifts, each image is normalized to a reference frame acquired at an

off-resonant MW frequency [59]. Multiple frequency sweeps are averaged, resulting in an effective integration time of approximately 100 ms per frequency point.

Pixel-wise Lorentzian fitting is subsequently applied to extract the resonance frequencies, and the corresponding frequency shifts are converted into two-dimensional maps of the N-V-projected stray magnetic field, $B_{\text{N-}V}$, enabling imaging of magnetic textures over extended FOVs.

APPENDIX B: EXPERIMENTAL SETUP

The N-V-based magnetic field measurements are performed using a custom-built inverted epifluorescence microscope [Fig. 6(a)]. A 532 nm diode laser (Laser Quantum, gem 532 nm) provides optical excitation of the N-V centers. To reduce pointing instability, the laser beam is coupled into a polarization-maintaining single-mode fiber (PMC-460Si-3-18E-150). A 50:50 beam-splitter cube directs the excitation light toward the sample and separates the reflected and PL signals. Imaging is performed with an air objective (Newport $\mathrm{M}-20\times$, $\mathrm{NA}=0.40$) with an effective focal length of 9 mm.

The sample assembly consists of a custom flexible printed circuit board (PCB) of thickness 0.11 mm incorporating an Ω-shaped MW stripline with a 3 mm central aperture. The PCB is mounted on a three-dimensional translation stage for precise positioning. A diamond sensor containing a near-surface N-V layer is placed on the PCB, and the magnetic sample is positioned directly on top of the diamond to minimize the sensor-sample stand-off distance. The diamond is oriented such that the N-V layer faces the magnetic film, maximizing magnetic sensitivity. The FOV is aligned with the center of the stripline loop to ensure uniform MW excitation.

To filter the N-V photoluminescence, a 650 nm long-pass filter (FEL0650, Thorlabs) is used. A flip mirror enables switching between imaging and point-detection configurations. Wide-field detection is performed using an sCMOS camera (Andor Zyla Wave 5.5 MP) with a camera sensor pixel size of 6.5 $\mu\mathrm{m}^2$, corresponding to an effective pixel size of approximately 325×325 nm^2 in the sample plane. For time-resolved or high-sensitivity measurements, an avalanche photodetector (APD440A, Thorlabs) is used, offering low dark counts and high quantum efficiency in the N-V emission band.

For wide-field N-V magnetometry, we use a high-density N-V ensemble located near the diamond surface. A 100-nm-thick layer of ^{14}N-doped, isotope-purified diamond (99.9 % ^{12}C) is grown via chemical vapor deposition on an electronic-grade diamond substrate provided by Element Six. To create vacancies, the sample is implanted with 25 keV He^+ ions at a dose of 10^{12} ions/cm^2, followed by vacuum annealing at 900°C for 2 h to form N-V centers. Subsequently, the sample undergoes annealing in O_2 at 425°C for 2 h to stabilize the charge state. The resulting N-V ensemble exhibits a density of approximately 1.2×10^{17} cm^{-3}, determined by comparing the fluorescence from this layer to that of near-surface single N-V centers in a reference sample. The diamond crystal has dimensions of 2×2 mm^2 with a thickness of around 90–100 μm [21,60].

Magnetic domains are tuned using a bias magnetic field B_z generated by a Helmholtz coil (radius = 4 cm)

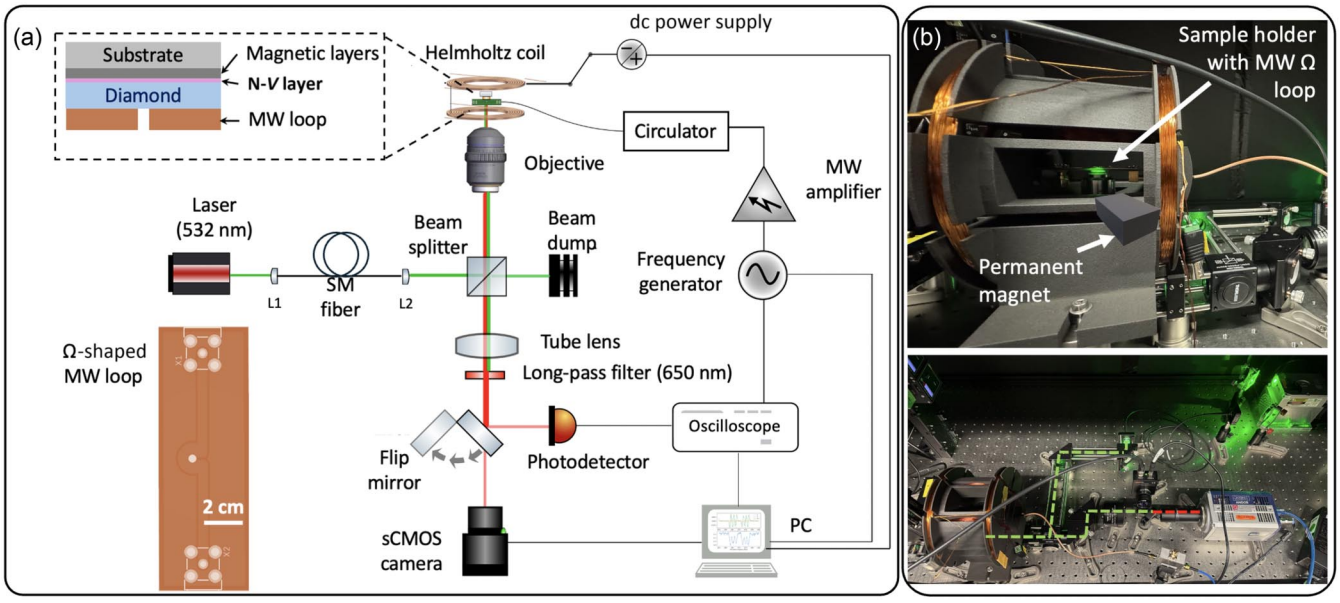


FIG. 6. Wide-field N-V magnetometry setup. (a) Schematic of the optical and MW setup. (b) Photographs of the experimental setup showing the sample holder with MW loop and the optical table configuration.

[Fig. 6(b)], providing a field of approximately 1 mT/A. The coil is driven by a computer-controlled dc power supply (Rigol DP-832), allowing magnetic field control with a resolution of approximately 10 μT during measurements. MW excitation for N-V magnetometry is provided by a signal generator (SRS SG384). The MW output is amplified using a 16 W (+43 dB) power amplifier (ZHL-16 W-43+) and routed through a circulator (Pasternack CS-3.000) before delivery to the 50 Ω-terminated Ω-shaped stripline integrated into the sample holder.

In addition to the OOP field, skyrmion nucleation requires an IP magnetic field component. This field is generated using a permanent magnet oriented parallel to the sample surface, producing an IP field of approximately 30 mT at a distance of 1 cm from the sample. The magnet is mounted on a lateral translation stage, allowing controlled and reversible application of the IP field. By adjusting its position, both the magnitude and direction of the IP field can be tuned without perturbing the optical alignment or overall experimental configuration.

The resulting skyrmions are expected to be predominantly Néel-type, stabilized by the interfacial DMI present in the multilayer stack. Such PMA multilayers are widely employed for stabilizing relatively large skyrmions and magnetic bubble textures [1,8].

The performance of the wide-field N-V magnetometer is characterized by its magnetic field sensitivity, which is estimated from both shot-noise considerations and experimental noise measurements. The ideal shot-noise-limited magnetic field sensitivity of the magnetometer is calculated using the expression [61]

$$\eta_{\mathrm{cw}} = \frac{4}{3\sqrt{3}} \cdot \frac{h}{g_e \mu_B} \cdot \frac{\Delta\nu}{C_{\mathrm{cw}}\sqrt{R}}, \tag{B1}$$

where $\Delta\nu$ is the ODMR linewidth, R is the detected photon count-rate, and C_{cw} denotes the cw-ODMR contrast. The prefactor $4/3\sqrt{3}$ arises from the maximum slope of a Lorentzian resonance profile. Apart from the fundamental constants (h, g_e, and μ_B), the sensitivity is governed by the ratio $\Delta\nu/C_{\mathrm{cw}}$, which reflects the sharpness of the ODMR resonance and its measurement contrast, as well as by $\sqrt{R}$. Using the experimentally determined parameters $\Delta\nu = 2.7$ MHz, $C_{\mathrm{cw}} = 4.5\%$, and $R = 1.85 \times 10^8$ counts/s, the ideal shot-noise-limited magnetic field sensitivity per pixel is estimated to be

$$\eta_{\mathrm{cw}}^{\mathrm{ideal}} \approx 0.1\ \mu\mathrm{T}/\sqrt{\mathrm{Hz}}.$$

Practically, however, the magnetic field sensitivity per pixel determined from the noise spectral density measurements yields

$$\eta_{\mathrm{cw}}^{\mathrm{exp}} \approx 10.0\text{–}20.0\ \mu\mathrm{T}/\sqrt{\mathrm{Hz}},$$

which is two orders of magnitude above the ideal shot-noise limit. To further quantify the origin of the discrepancy between the ideal and experimental sensitivity, we note that the dominant noise contributions arise from a combination of camera readout noise, laser intensity fluctuations, and MW amplitude/frequency instability. Based on the measured noise spectral density, the effective magnetic field noise floor per pixel is on the order of approximately 10 $\mu\mathrm{T}/\sqrt{\mathrm{Hz}}$. Among these contributions, technical noise sources (laser and MW fluctuations) dominate over photon shot noise under the present operating conditions. This noise level sets the minimum detectable magnetic field variation in the reconstructed images. For an effective integration time (T) of approximately 100 ms per frequency point, the magnetic field noise per pixel is estimated as $\sigma_B \approx \eta/\sqrt{T} \approx 30\text{–}60$ μT. Given that the typical stray-field contrast associated with skyrmions is on the order of 0.3–1 mT, this corresponds to a signal-to-noise ratio of roughly 5–30, which is sufficient to reliably resolve skyrmion features. Consequently, under the present measurement conditions, the extraction of skyrmion properties is generally more strongly limited by spatial resolution and segmentation accuracy than by magnetic sensitivity.

However, the finite sensitivity contributes to uncertainty in the precise determination of skyrmion boundaries, particularly for low-contrast regions or near the edges of the skyrmions, where the magnetic field gradients are smaller. This leads to a small systematic uncertainty in the extracted geometrical parameters, which is mitigated in the present work by statistical averaging over large skyrmion ensembles.

The finite N-V-sample stand-off distance and the spatial extent of the N-V layer lead to a convolution of the measured magnetic field, effectively smoothing high-spatial-frequency features, slightly overestimating characteristic length scales, and reducing peak field amplitudes. To determine the N-V-sample separation, we fit the measured stray-field profiles across DWs using the analytical two-edge stripe model [62], where a uniformly OOP magnetized domain is modeled as two anti-parallel bound currents at its edges and the resulting field is projected onto the N-V axis. The stand-off distance z is obtained as a fitting parameter and represents an effective magnetic distance that includes both the physical gap and the finite N-V depth distribution, yielding a value of $z \approx 1\text{–}2$ μm, consistent with the average magnetic domain width of approximately 6 μm. This extracted value is in good agreement with the experimentally observed magnetic field profiles.

APPENDIX C: SAMPLE PREPARATION AND MOLECULAR FUNCTIONALIZATION

To selectively functionalize the magnetic thin films while retaining an internal reference region, each sample was first coated with a protective PMMA layer. One half of the sample surface was subsequently masked using Kapton tape, and the exposed region was cleaned by dissolving the PMMA in acetone, producing a well-defined boundary between protected and unprotected regions.

After removal of the Kapton mask, the samples were immersed overnight in 1 mM solutions containing either D-AHPA or L-AHPA molecules, enabling selective adsorption on the exposed Au surface. The molecules bind to the gold surface via chemisorption of the terminal cysteine thiol group (Au—S bond) and adopt a tilted orientation with an angle of approximately 46° relative to the surface normal [63]. The resulting self-assembled monolayer provides dense surface coverage with an intermolecular spacing of approximately 12 Angstrom and remains stable against brief acetone exposure at room temperature.

Finally, the remaining PMMA layer was removed by a short acetone bath (approximately 2 min), yielding samples containing adjacent molecule-functionalized and nonfunctionalized regions on the same substrate. Because the two enantiomers are chemically identical and undergo identical processing procedures, differences between D- and L-functionalized samples are unlikely to originate solely from ordinary surface-treatment effects.

APPENDIX D: STATISTICAL SUMMARY

The table below provides the complete statistical summary supporting the quantitative analysis presented in Sec. VI. The statistics compare skyrmion properties in molecule-functionalized and adjacent nonfunctionalized (bare) regions under opposite OOP magnetic field polarities ($B_z = \pm 1.6$ mT).

TABLE I. Statistical summary of all measured quantities. Group means are reported with 95% CI. Variance, mean difference, relative change, Mann-Whitney p-value, and Cohen's d are included to facilitate comparison between adjacent bare and molecule-functionalized regions.

Polarity	Metric	Group 1	Group 1 mean (95% CI)	Group 1 total skyrmions	Group 1 var within/between cycle	Group 2	Group 2 mean (95% CI)	Group 2 total skyrmions	Group 2 var within/between cycle	Mean difference (95% CI)	Relative change mean ± SEM	Mann-Whitney p	Cohen d (95% CI)
+Bz	Density (μm^{-2})	D-AHPA	0.53 (0.36 to 0.69)	3329	0.03 / 0.00	Bare (D-AHPA)	0.42 (0.10 to 0.74)	2668	0.03 / 0.11	0.10 (-0.12 to 0.39)	0.25 ± 0.16	0.82	0.42
	Diameter (μm)		1.46 (1.26 to 1.67)		0.05 / 0.00		1.33 (1.05 to 1.61)		0.04 / 0.07	0.13 (-0.09 to 0.41)	0.10 ± 0.06	0.48	0.56
	Shape factor		0.07 (0.07 to 0.07)		0.00 / 0.00		0.07 (0.06 to 0.08)		0.00 / 0.00	0.01 (-0.00 to 0.01)	0.07 ± 0.02	0.59	0.70
	Spacing (μm)		4.94 (4.71 to 5.17)		0.05 / 0.01		6.36 (3.55 to 9.17)		4.41 / 6.09	-1.42 (-3.88 to 0.23)	-0.22 ± 0.01	0.82	-0.75
-Bz	Density (μm^{-2})		0.32 (0.18 to 0.46)	2045	0.02 / 0.00		0.49 (0.23 to 0.74)	3084	0.03 / 0.06	-0.16 (-0.34 to 0.08)	-0.34 ± 0.11	0.18	-0.84
	Diameter (μm)		1.41 (1.29 to 1.53)		0.02 / 0.00		1.39 (1.24 to 1.53)		0.02 / 0.01	0.03 (-0.12 to 0.14)	0.02 ± 0.04	0.94	0.20
	Shape factor		0.07 (0.07 to 0.07)		0.00 / 0.00		0.07 (0.06 to 0.07)		0.00 / 0.00	0.00 (-0.00 to 0.01)	0.04 ± 0.01	0.59	0.50
	Spacing (μm)		5.38 (5.00 to 5.76)		0.13 / 0.04		5.59 (3.59 to 7.59)		3.46 / 1.45	-0.21 (-2.59 to 0.69)	-0.04 ± 0.03	0.07	-0.15
+Bz	Density (μm^{-2})	L-AHPA	0.19 (0.01 to 0.37)	1209	0.01 / 0.04	Bare (L-AHPA)	0.38 (0.14 to 0.63)	2416	0.03 / 0.05	-0.19 (-0.39 to 0.03)	-0.50 ± 0.18	0.18	-0.94
	Diameter (μm)		1.35 (1.26 to 1.44)		0.01 / 0.00		1.43 (1.13 to 1.72)		0.03 / 0.10	-0.07 (-0.33 to 0.11)	-0.05 ± 0.03	0.82	-0.36
	Shape factor		0.07 (0.06 to 0.07)		0.00 / 0.00		0.07 (0.06 to 0.07)		0.00 / 0.00	-0.00 (-0.01 to 0.01)	-0.00 ± 0.04	1.00	-0.04
	Spacing (μm)		7.93 (4.14 to 11.72)		7.23 / 12.13		6.42 (3.68 to 9.16)		6.00 / 3.38	1.51 (-1.51 to 5.07)	0.23 ± 0.23	0.31	0.48
-Bz	Density (μm^{-2})		0.27 (-0.02 to 0.56)	1718	0.06 / 0.05		0.16 (0.05 to 0.28)	1030	0.01 / 0.00	0.11 (-0.07 to 0.40)	0.67 ± 0.70	0.82	0.51
	Diameter (μm)		1.30 (1.08 to 1.52)		0.04 / 0.01		1.48 (1.30 to 1.66)		0.03 / 0.01	-0.18 (-0.40 to 0.01)	-0.12 ± 0.06	0.31	-0.94
	Shape factor		0.06 (0.06 to 0.07)		0.00 / 0.00		0.06 (0.06 to 0.07)		0.00 / 0.00	0.00 (-0.01 to 0.01)	0.02 ± 0.06	0.82	0.18
	Spacing (μm)		6.55 (4.95 to 8.16)		1.54 / 1.85		7.66 (5.95 to 9.37)		2.96 / 0.48	-1.11 (-2.85 to 0.46)	-0.14 ± 0.08	0.31	-0.70

[1] A. Fert, V. Cros, and J. Sampaio, Skyrmions on the track, Nat. Nanotechnol. **8**, 152 (2013).

[2] A. Bogdanov and A. Hubert, Thermodynamically stable magnetic vortex states in magnetic crystals, J. Magn. Magn. Mater. **138**, 255 (1994).

[3] S. Heinze, K. von Bergmann, M. Menzel, J. Brede, A. Kubetzka, R. Wiesendanger, G. Bihlmayer, and S. Blügel, Spontaneous atomic-scale magnetic skyrmion lattice in two dimensions, Nat. Phys. **7**, 713 (2011).

[4] T. H. R. Skyrme, A non-linear field theory, Proc. R. Soc. A **260**, 127 (1961).

[5] H. Zhang, Y. Zhang, Z. Hou, M. Qin, X. Gao, and J. Liu, Magnetic Skyrmions: Materials, manipulation, detection, and applications in spintronic devices, Mater. Futures **2**, 032201 (2023).

[6] K. Everschor-Sitte, J. Masell, R. M. Reeve, and M. Kläui, Perspective: Magnetic Skyrmions—overview of recent progress in an active research field, J. Appl. Phys. **124**, 240901 (2018).

[7] L. Li, D. Song, W. Wang, L. Kong, S. Zhang, N. Wang, S. Zhang, M. Tian, J. Zang, Y. Liu, and H. Du, Electrically writing a magnetic Heliknoton in a chiral magnet, Nat. Mater. **25**, 950 (2026).

[8] N. Nagaosa and Y. Tokura, Topological properties and dynamics of magnetic Skyrmions, Nat. Nanotechnol. **8**, 899 (2013).

[9] A. Fert, N. Reyren, and V. Cros, Magnetic Skyrmions: Advances in physics and potential applications, Nat. Rev. Mater. **2**, 17031 (2017).

[10] C. Reichhardt, C. J. O. Reichhardt, and M. V. Milošević, Statics and dynamics of Skyrmions interacting with disorder and nanostructures, Rev. Mod. Phys. **94**, 035005 (2022).

[11] S. Jaiswal, K. Lee, J. Langer, B. Ocker, M. Kläui, and G. Jakob, Tuning of interfacial perpendicular magnetic anisotropy and domain structures in magnetic thin film multilayers, J. Phys. D: Appl. Phys. **52**, 295002 (2019).

[12] Z. Shen, C. Song, Y. Xue, Z. Wu, J. Wang, and Z. Zhong, Strain-tunable Dzyaloshinskii-Moriya interaction and Skyrmions in two-dimensional Janus $Cr_2X_3Y_3(X, Y = Cl, Br, I, X \neq Y)$ trihalide monolayers, Phys. Rev. B **106**, 094403 (2022).

[13] T. Dohi, R. M. Reeve, and M. Kläui, Thin film skyrmionics, Annu. Rev. Condens. Matter Phys. **13**, 73 (2022).

[14] R. Naaman, Y. Paltiel, and D. H. Waldeck, Chiral molecules and the electron spin, Nat. Rev. Chem. **3**, 250 (2019).

[15] O. B. Dor, S. Yochelis, A. Radko, K. Vankayala, E. Capua, A. Capua, S. Yang, L. T. Baczewski, S. S. P. Parkin, R. Naaman *et al.*, Magnetization switching in ferromagnets by adsorbed chiral molecules without current or external magnetic field, Nat. Commun. **8**, 14567 (2017).

[16] M. R. Safari, F. Matthes, V. Caciuc, N. Atodiresei, C. M. Schneider, K. Ernst, and D. E. Bürgler, Enantioselective adsorption on magnetic surfaces, Adv. Mater. **36**, 2308666 (2024).

[17] Y. Kapon, F. Kammerbauer, T. Balland, S. Yochelis, M. Kläui, and Y. Paltiel, Effects of chiral polypeptides on Skyrmion stability and dynamics, Nano Lett. **25**, 306 (2025).

[18] Y. Kapon, F. Kammerbauer, S. Yochelis, M. Kläui, and Y. Paltiel, Magneto-optical imaging of magnetic-domain pinning induced by chiral molecules, J. Chem. Phys. **159**, 064701 (2023).

[19] L. Rondin, J.-P. Tetienne, T. Hingant, J.-F. Roch, P. Maletinsky, and V. Jacques, Magnetometry with nitrogen-vacancy defects in diamond, Rep. Prog. Phys. **77**, 056503 (2014).

[20] E. V. Levine, M. J. Turner, P. Kehayias, C. A. Hart, N. Langellier, R. Trubko, D. R. Glenn, R. R. Fu, and R. L. Walsworth, Principles and techniques of the quantum diamond microscope, Nanophotonics **8**, 1945 (2019).

[21] T. Lenz, G. Chatzidrosos, Z. Wang, L. Bougas, Y. Dumeige, A. Wickenbrock, N. Kerber, J. Zázvorka, F. Kammerbauer, M. Kläui *et al.*, Imaging topological spin structures using light-polarization and magnetic microscopy, Phys. Rev. Appl. **15**, 024040 (2021).

[22] K. G. Rana, A. Finco, F. Fabre, S. Chouaieb, A. Haykal, L. D. Buda-Prejbeanu, O. Fruchart, S. Le Denmat, P. David, M. Belmeguenai *et al.*, Room-temperature Skyrmions at zero field in exchange-biased ultrathin films, Phys. Rev. Appl. **13**, 044079 (2020).

[23] S. Vélez, S. Ruiz-Gómez, J. Schaab, E. Gradauskaite, M. S. Wörnle, P. Welter, B. J. Jacot, C. L. Degen, M. Trassin, M. Fiebig *et al.*, Current-driven dynamics and ratchet effect of Skyrmion bubbles in a ferrimagnetic insulator, Nat. Nanotechnol. **17**, 834 (2022).

[24] I. Gross, W. Akhtar, A. Hrabec, J. Sampaio, L. J. Martinez, S. Chouaieb, B. J. Shields, P. Maletinsky, A. Thiaville, S. Rohart *et al.*, Skyrmion morphology in ultrathin magnetic films, Phys. Rev. Mater. **2**, 024406 (2018).

[25] Y. Dovzhenko, F. Casola, S. Schlotter, T. X. Zhou, F. Büttner, R. L. Walsworth, G. S. D. Beach, and A. Yacoby, Magnetostatic twists in room-temperature Skyrmions explored by nitrogen-vacancy center spin texture reconstruction, Nat. Commun. **9**, 2712 (2018).

[26] A. Jenkins, M. Pelliccione, G. Yu, X. Ma, X. Li, K. L. Wang, and A. C. B. Jayich, Single-spin sensing of domain-wall structure and dynamics in a thin-film Skyrmion host, Phys. Rev. Mater. **3**, 083801 (2019).

[27] D. A. Simpson, J.-P. Tetienne, J. M. McCoey, K. Ganesan, L. T. Hall, S. Petrou, R. E. Scholten, and L. C. L. Hollenberg, Magneto-optical imaging of thin magnetic films using spins in diamond, Sci. Rep. **6**, 22797 (2016).

[28] D. Le Sage, K. Arai, D. R. Glenn, S. J. DeVience, L. M. Pham, L. Rahn-Lee, M. D. Lukin, A. Yacoby, A. Komeili, and R. L. Walsworth, Optical magnetic imaging of living cells, Nature (London) **496**, 486 (2013).

[29] Y. Schlussel, T. Lenz, D. Rohner, Y. Bar-Haim, L. Bougas, D. Groswasser, M. Kieschnick, E. Rozenberg, L. Thiel, A. Waxman *et al.*, Wide-field imaging of superconductor vortices with electron spins in diamond, Phys. Rev. Appl. **10**, 034032 (2018).

[30] A. Nowodzinski, M. Chipaux, L. Toraille, V. Jacques, J.-F. Roch, and T. Debuisschert, Nitrogen-vacancy centers in diamond for current imaging at the redistributive layer level of integrated circuits, Microelectron. Reliab. **55**, 1549 (2015).

[31] S. E. Lillie, N. Dontschuk, D. A. Broadway, D. L. Creedon, L. C. L. Hollenberg, and J.-P. Tetienne, Imaging graphene field-effect transistors on diamond using nitrogen-vacancy microscopy, Phys. Rev. Appl. **12**, 024018 (2019).

[32] F. Casola, T. van der Sar, and A. Yacoby, Probing condensed matter physics with magnetometry based on nitrogen-vacancy centres in diamond, Nat. Rev. Mater. **3**, 1 (2018).

[33] J. Shaji Rebeirro, M. Omar, T. Lenz, O. Dhungel, P. Blümler, D. Budker, and A. Wickenbrock, Microwave-free wide-field magnetometry using nitrogen-vacancy centers, Phys. Rev. Appl. **21**, 044039 (2024).

[34] S. Sengottuvel, O. Dhungel, M. Mrózek, A. Wickenbrock, D. Budker, W. Gawlik, and A. M. Wojciechowski, Microwave-free imaging magnetometry with nitrogen-vacancy centers in nanodiamonds at near-zero field, Phys. Rev. Appl. **23**, 034001 (2025).

[35] T. Lancaster, Skyrmions in magnetic materials, Contemp. Phys. **60**, 246 (2019).

[36] F. Büttner and M. Kläui, Magnetic skyrmion dynamics, in *Skyrmions: Topological Structures, Properties, and Applications*, edited by J. Ping Liu, Z. Zhang, and G. Zhao (CRC Press, Boca Raton, Florida, USA, 2016), pp. 211–238, 10.1201/9781315284170-9.

[37] U. K. Rößler, A. N. Bogdanov, and C. Pfleiderer, Spontaneous Skyrmion ground states in magnetic metals, Nature (London) **442**, 797 (2006).

[38] S. Mühlbauer, B. Binz, F. Jonietz, C. Pfleiderer, A. Rosch, A. Neubauer, R. Georgii, and P. Böni, Skyrmion lattice in a chiral magnet, Science **323**, 915 (2009).

[39] X. Z. Yu, Y. Onose, N. Kanazawa, J. H. Park, J. H. Han, Y. Matsui, N. Nagaosa, and Y. Tokura, Real-space observation of a two-dimensional Skyrmion crystal, Nature (London) **465**, 901 (2010).

[40] S. Seki, X. Z. Yu, S. Ishiwata, and Y. Tokura, Observation of Skyrmions in a multiferroic material, Science **336**, 198 (2012).

[41] A. K. Nayak, V. Kumar, T. Ma, P. Werner, E. Pippel, R. Sahoo, F. Damay, U. K. Rößler, C. Felser, and S. S. P. Parkin, Magnetic antiskyrmions above room temperature in tetragonal Heusler materials, Nature (London) **548**, 561 (2017).

[42] N. Romming, C. Hanneken, M. Menzel, J. E. Bickel, B. Wolter, K. von Bergmann, A. Kubetzka, and R. Wiesendanger, Writing and deleting single magnetic Skyrmions, Science **341**, 636 (2013).

[43] L. D. Barron, True and false chirality and absolute asymmetric synthesis, J. Am. Chem. Soc. **108**, 5539 (1986).

[44] R. Naaman and D. H. Waldeck, Spintronics and chirality: Spin selectivity in electron transport through chiral molecules, Annu. Rev. Phys. Chem. **66**, 263 (2015).

[45] R. Naaman, Y. Paltiel, and D. H. Waldeck, Chirality and spin: A different perspective on enantioselective interactions, Chimia **72**, 394 (2018).

[46] B. P. Bloom, Y. Paltiel, R. Naaman, and D. H. Waldeck, Chiral-induced spin selectivity, Chem. Rev. **124**, 1950 (2024).

[47] A. Moharana, Y. Kapon, F. Kammerbauer, D. Anthofer, S. Yochelis, H. Shema, E. Gross, M. Kläui, Y. Paltiel, and A. Wittmann, Chiral-induced unidirectional spin-to-charge conversion, Sci. Adv. **11**, eado4285 (2025).

[48] J.-P. Tetienne, T. Hingant, L. J. Martinez, S. Rohart, A. Thiaville, L. H. Diez, K. Garcia, J.-P. Adam, J.-V. Kim, J.-F. Roch *et al.*, The nature of domain walls in ultrathin ferromagnets revealed by scanning nanomagnetometry, Nat. Commun. **6**, 6733 (2015).

[49] I. Labrie-Boulay, T. B. Winkler, D. Franzen, A. Romanova, H. Fangohr, and M. Kläui, Machine-learning-based detection of spin structures, Phys. Rev. Appl. **21**, 014014 (2024).

[50] T. B. Winkler, I. Labrie-Boulay, A. Romanova, H. Fangohr, M. Kläui, R. Gruber, F. Kammerbauer, K. Raab, J. Zazvorka, and K. Leutner, Moke-microscopy-Skyrmion-dataset (2024).

[51] S. Rohart and A. Thiaville, Skyrmion confinement in ultrathin film nanostructures in the presence of Dzyaloshinskii-Moriya interaction, Phys. Rev. B **88**, 184422 (2013).

[52] B. Hondamuni, Wide-field N*V* magnetometry data, [Data & codes], Zenodo (2026). 10.5281/zenodo.22929570.

[53] P. Welter, J. Rhensius, A. Morales, M. S. Wörnle, C.-H. Lambert, G. Puebla-Hellmann, P. Gambardella, and C. L. Degen, Scanning nitrogen-vacancy center magnetometry in large in-plane magnetic fields, Appl. Phys. Lett. **120**, 074003 (2022).

[54] W. Pfaff, B. J. Hensen, H. Bernien, S. B. van Dam, M. S. Blok, T. H. Taminiau, M. J. Tiggelman, R. N. Schouten, M. Markham, D. J. Twitchen *et al.*, Unconditional quantum teleportation between distant solid-state quantum bits, Science **345**, 532 (2014).

[55] M. W. Doherty, N. B. Manson, P. Delaney, F. Jelezko, J. Wrachtrup, and L. C. L. Hollenberg, The nitrogen-vacancy colour centre in diamond, Phys. Rep. **528**, 1 (2013).

[56] S. Hayami and Y. Motome, Topological spin crystals by itinerant frustration, J. Phys.: Condens. Matter **33**, 443001 (2021).

[57] M. Morgenbesser, S. Taibl, M. Kubicek, A. Schmid, A. Viernstein, N. Bodenmüller, C. Herzig, F. Baiutti, J. de Dios Sirvent, M. O. Liedke *et al.*, Cation non-stoichiometry in Fe: $SrTiO_3$ thin films and its effect on the electrical conductivity, Nanoscale Adv. **3**, 6114 (2021).

[58] P. Tamarat, T. Gaebel, J. R. Rabeau, M. Khan, A. D. Greentree, H. Wilson, L. C. L. Hollenberg, S. Prawer, P. Hemmer, F. Jelezko *et al.*, Stark shift control of single optical centers in diamond, Phys. Rev. Lett. **97**, 083002 (2006).

[59] S. C. Scholten, A. J. Healey, I. O. Robertson, G. J. Abrahams, D. A. Broadway, and J.-P. Tetienne, Widefield quantum microscopy with nitrogen-vacancy centers in diamond: Strengths, limitations, and prospects, J. Appl. Phys. **130**, 150902 (2021).

[60] E. E. Kleinsasser, M. M. Stanfield, J. K. Q. Banks, Z. Zhu, W. Li, V. M. Acosta, H. Watanabe, K. M. Itoh, and K. C. Fu, High density nitrogen-vacancy sensing surface created via He^+ ion implantation of ^{12}C diamond, Appl. Phys. Lett. **108**, 202401 (2016).

[61] J. F. Barry, J. M. Schloss, E. Bauch, M. J. Turner, C. A. Hart, L. M. Pham, and R. L. Walsworth, Sensitivity optimization for N*V*-diamond magnetometry, Rev. Mod. Phys. **92**, 015004 (2020).

[62] Z. Xu, M. L. Palm, W. Huxter, K. Herb, J. M. Abendroth, K. Bouzehouane, O. Boulle, M. S. Gabor, J. U. Larranaga, A. Morales *et al.*, Minimizing sensor-sample distances in scanning nitrogen-vacancy magnetometry, ACS Nano **19**, 8255 (2025).

[63] T. N. H. Nguyen, L. Rasabathina, O. Hellwig, A. Sharma, G. Salvan, S. Yochelis, Y. Paltiel, L. T. Baczewski, and C. Tegenkamp, Cooperative effect of electron spin polarization in chiral molecules studied with non-spin-polarized scanning tunneling microscopy, ACS Appl. Mater. Interfaces **14**, 38013 (2022).